Enhanced Low-Frequency Monopole and Dipole Acoustic Antennas Based on a Subwavelength Bianisotropic Structure

Yurou Jia, Yanchun Luo, Dajian Wu,* Qi Wei, and Xiaojun Liu*

High-efficiency sound emission is crucial in practical scenarios, such as sonar system and acoustic communication. However, the efficient emission of the low-frequency sound source is difficult because of the large acoustic radiation reactance from the ambient medium. Here, a subwavelength bianisotropic hybrid Mie resonator (BHMR) is proposed, which has shown excellent capability in converting a central monopole source into the enhanced monopole and dipole acoustic antennas at low frequency. The simulated acoustic field distributions and far-field radiations of the BHMR demonstrate that the enhanced omnidirectional and directional antennas are induced by the monopole and dipole resonances, respectively. A BHMR sample is further fabricated and the enhancements of the monopole and dipole acoustic antennas by the BHMR are experimentally verified. The miniature BHMR offers an alternative way to achieve the enhanced low-frequency monopole and dipole antennas that are highly desirable for loudspeaker design and acoustic communication.

1. Introduction

Acoustic emissions have demonstrated great importance in various applications including focused sound waves for medical treatment,[1] target localization by sonar system,[2] and directional sound launch and reception in acoustic communication.[3] However, at low frequency range, sound emission efficiency is extremely low since the majority of the radiated energy is stored in near field due to the large acoustic radiation reactance.[4,5] The recent developed acoustic metamaterials,

such as space-coiling metamaterial cavity with Fabry–Perot resonances[6] and maze-like anisotropic enclosure with Mie resonances,[7,8] were utilized to greatly enhance the low-frequency monopole and dipole radiations. Then, Fan et al. enabled a dipole antenna from a monopole source by a subwavelength hybrid structure and the radiation efficiency is up to 2.3.[9] More recently, Liu et al.[10] proposed a cylindrical hyperlens-like structure with a central monopole source to realize enhanced monopole emissions at low frequency, while an eccentric monopole source is used to achieve enhanced multipole directional antennas.

In recent years, acoustic bianisotropic metamaterials (BMs) have attracted immense interest and have been explored in both fundamental and application researches.[11–13] The acoustic BM is commonly implemented by asymmetric structural units where the constitutive relations are coupled.[11,14] The field coupling in the acoustic BM is referred as Willis coupling that includes the strain-velocity coupling in elasticity[15] or the pressure-velocity coupling in acoustics.[16] The Willis coupling offers a new freedom for acoustic wave manipulation and has produced many fascinating applications.[17–23] For example, Koo et al. designed an acoustic BM to realize the pressure-velocity impedance conversion for independent control of the reflection and transmission angles.[12] By combining the properties of acoustic Willis coupling with *PT*-symmetric systems, a unidirectional reflectionless acoustic propagation was achieved.[18] Acoustic BMs were also employed as effective sound barriers to prevent sound diffractions in low-frequency noise control.[19] Li et al. further used gradient acoustic BMs to realize scattering-free wavefront manipulation[20] and high-efficient angular momentum transformation.[21]

In this work, we first design a subwavelength bianisotropic hybrid Mie resonantor (BHMR) that realizes both enhanced monopole and dipole acoustic antennas by putting a monopole source in it. The acoustic field distributions and the far-field radiations of the monopole and dipole modes of BHMRs are numerically investigated using finite element method. It is demonstrated that the enhanced monopole and dipole acoustic antennas arise from the acoustic resonances and Willis couplings of the BHMR. In addition, the influence of the structure size of the BHMR on the monopole and dipole resonance frequencies is discussed. Finally, we fabricate a

Y. Jia, Y. Luo, Prof. D. Wu, Dr. Q. Wei
Jiangsu Key Lab on Opto-Electronic Technology
School of Physics and Technology
Nanjing Normal University
Nanjing 210023, China
E-mail: wudajian@njnu.edu.cn
Prof. D. Wu, Prof. X. Liu
Key Laboratory of Modern Acoustics
Nanjing University
Nanjing 210093, China
E-mail: liuxiaojun@nju.edu.cn

**ADVANCED
SCIENCE NEWS**
www.advancedsciencenews.com

**ADVANCED
MATERIALS
TECHNOLOGIES**
www.advmattechnol.de

BHMR sample and verify the enhanced monopole and dipole acoustic antennas experimentally.

2. Structure Design of Bianisotropic Hybrid Mie Resonantor

Figure 1a shows the schematic illustration of a 2D subwavelength BHMR with zigzag channels. The outer radius of BHMR is R, the wall thickness is $t = 0.035R$, and the channel width is $w = 0.05R$. The BHMR includes upper and lower parts: the lower half part with three fanlike labyrinth structures (FLSs) is split from the traditional six-channel Mie resonator (SMR), while the upper half part with five FLSs comes from the ten-channel Mie resonator (TMR). Figure 1b,c shows the schematic diagrams of an SMR and a TMR, respectively.[24,25] The SMR and TMR share the same structure parameters (R, t, w) with the BHMR. The curling number N of the FLS in SMR is same as that of the FLS in TMR. Here, the curling number N describes how many times sound waves circulate in zigzag channels. Thus, the inner radius of BHMR is $R_i = R - N(t + w) - t$. When sound waves propagate along the zigzag channels, the effective acoustic path is elongated. In an FLS, the sound path length along the channel is $L = R - R_i + \{2\pi N[R_i + t + 0.5w + (N-1)(w+t)/2] - M(t+w)\}/M$, M is the number of the FLS in a Mie resonator. Based on the effective medium theory, SMR and TMR can be characterized by the effective radial sound speed c_r and anisotropic effective mass density tensor $\rho = \mathrm{diag}[\rho_r, \rho_\theta]$[8,25]

$$\begin{cases} c_r = \dfrac{(R - R_i)}{L} c_0 \\ \rho_r = \dfrac{2\pi L r}{M w (R - R_i)} \rho_0, \quad (R_i \le r \le R) \\ \rho_\theta \to \infty \end{cases} \quad (1)$$
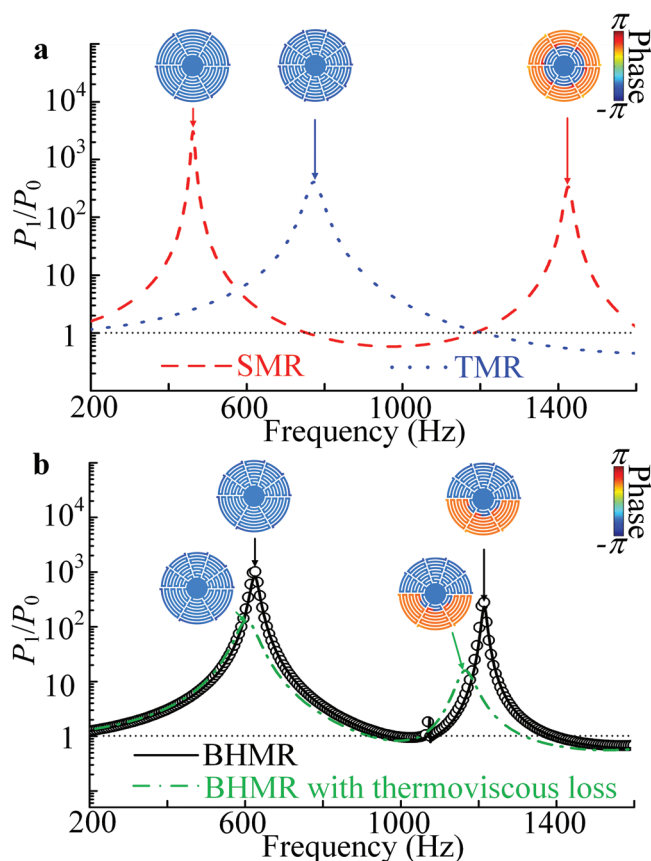
where ρ_0 and c_0 are the mass density and sound velocity of the background medium. Throughout this paper, the curling number N is fixed at 8. We consider a monopole source with maximum pressure and null velocity placed at the center of a Mie resonantor, as shown in Figure 1d. It is known the monopole and dipole moments are dominant in the scattered fields for subwavelength scatters.[14–16] For SMR or TMR, the monopole and dipole moments are proportional to the local pressure field and local velocity, respectively.[16,17] Therefore, under the excitation of a central monopole source, the purely pressure field induces only a monopole resonance in SMR or TMR and the dipole mode is prohibited, as shown in Figure 1e. Here, 2A denotes the total acoustic pressure coming out from the Mie resonator. At the monopole resonance, the radiation resistance reaches maximum and the radiation reactance is ≈0, resulting in the enhanced monopole emissions.[7,8] For a BHMR, the local pressure and velocity fields interact with each other because of the Willis coupling between the upper and lower parts, and therefore both pressure and velocity fields can excite monopole and dipole moments, as shown in Figure 1f.[16,17] Here, 2A and 2B indicate the total acoustic pressures coming out from the upper and lower parts of the BHMR, respectively. By decomposing 2A into (A+B) and (A−B) and 2B into (A+B) and −(A−B), the overall acoustic responses of the BHMR are decomposed into the monopole and dipole modes.[16,17] The structure configuration for BHMR is a direct "addition" of the half parts from the SMR and TMR, but the monopole and dipole modes of the BHMR are due to the Willis coupling between the upper and lower parts. The Willis coupling in BMs enriches the scattered fields and provides more possibilities for acoustic wave manipulations. So far, the acoustic BMs have been employed to realize various fascinating phenomena, such as acoustic unidirectional zero reflection, broadband sound barriers, and scattering-free wave manipulation.[18–21] However, the structure design based on acoustic BMs has not been applied in acoustic antennas. In this work, we would like to unite acoustic Willis coupling and acoustic resonances in BHMR to realize both enhanced monopole and dipole antennas.
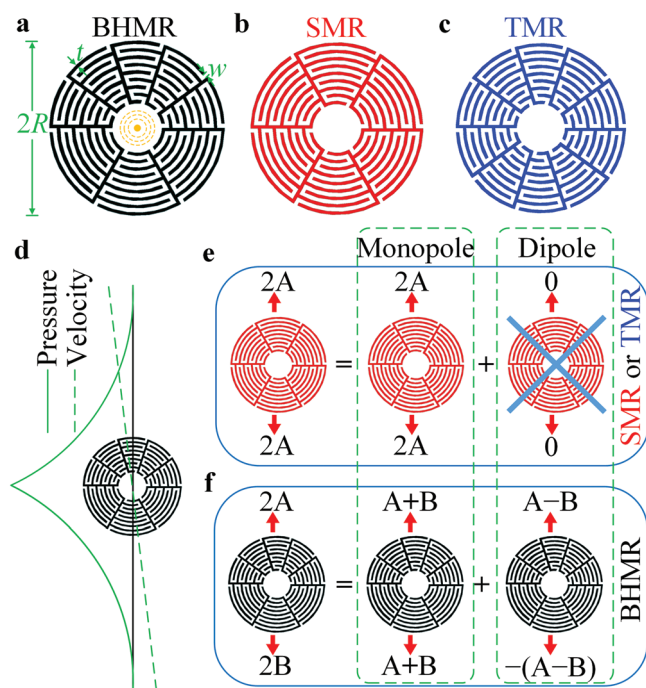
Figure 1. a) Schematic of a 2D subwavelength bianisotropic hybrid Mie resonator (BHMR). Schematic diagrams of b) a six-channel Mie resonator (SMR) and c) a ten-channel Mie resonator (TMR). d) A monopole source with maximum pressure and null velocity placed at the center of a Mie resonator. e) Physical interpretation of the monopole response of SMR or TMR. f) Physical interpretation of the monopole and dipole responses of the BHMR.

3. Performance of Bianisotropic Hybrid Mie Resonantor

We first numerically investigate the radiation characteristics of Mie resonators using finite element method (COMSOL Multiphysics software). The frameworks of Mie resonantors are modeled as acoustically rigid. The structure parameters are set as $R = 30$ mm, $t = 1.05$ mm, and $w = 1.5$ mm. The background medium is air with mass density $\rho_{\mathrm{air}} = 1.21$ kg m^{-3} and sound velocity $c_{\mathrm{air}} = 343.2$ m s^{-1}. A monopole source is

ADVANCED
SCIENCE NEWS
www.advancedsciencenews.com

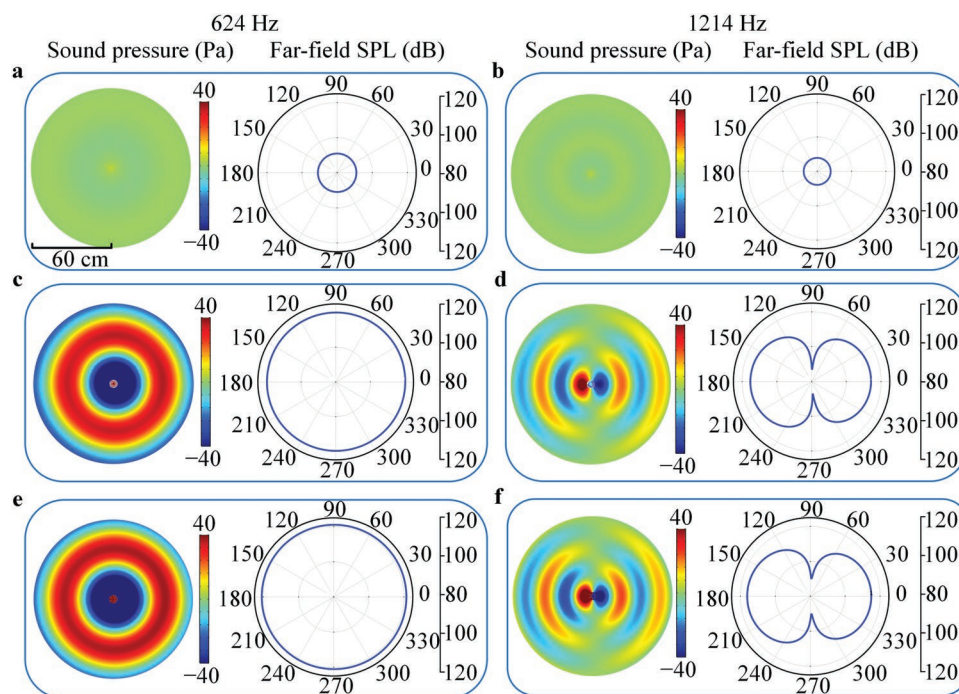**ADVANCED**
MATERIALS
TECHNOLOGIES
www.advmattechnol.de

Figure 2. a) Acoustic enhanced efficiency (P_1/P_0) of the SMR (dashed line) and TMR (dotted line) as a function of frequency. b) Acoustic enhanced efficiency (P_1/P_0) of a BHMR structure (solid and dashed–dotted lines) and the equivalent BHMR (circle scatters) as a function of frequency. The solid and dashed–dotted lines represent the simulated results without and with considering the thermoviscous effects, respectively.

located at the center of Mie resonantors. Perfectly matched layers are imposed on the outer boundaries to eliminate sound reflections. In **Figure 2**a, the dashed and dotted lines represent the acoustic enhanced efficiency (P_1/P_0) of the SMR and TMR as a function of frequency, respectively. Here, P_1 and P_0 are the far-field-radiated sound power with structure and the free-field-radiated sound power, respectively, which are calculated by integrating sound energy flux over a cylindrical surface ($r = 40$ mm).[7,10] For TMR, the peak at about 772 Hz arises from the monopole Mie resonance and the corresponding emission enhancement (P_1/P_0) can reach to ≈407. For SMR, it is observed that two peaks appear at about 462 and 1426 Hz, which arise from the monopole and second monopole Mie resonances, respectively.[8,24] The corresponding phase distributions of acoustic fields in TMR and SMR at resonances are given in the insets of Figure 2a. For TMR at 772 Hz, the sound waves in the zigzag channels vibrate with equal phases, which show a pattern of monopolar distribution. For SMR at 462 Hz, the phases of sound pressure are identical in all directions, which correspond to the monopole Mie resonances. At 1426 Hz, a π-phase difference between the inner and outer phase profiles is

observed but the phases of sound pressure still distribute equally in all directions of the SMR, which shows a pattern of the second monopole Mie resonances.[8,24] These properties of the monopole and second monopole Mie resonances of SMR are consistent with the results in the previous reports.[7,8] The solid line in Figure 2b shows the variation of the acoustic enhanced efficiency (P_1/P_0) of a BHMR structure with frequency, which matches well with the result of the equivalent BHMR based on Equation (1) (circle scatters). Two distinct peaks appear at ≈624 and ≈1214 Hz with the corresponding (P_1/P_0)-values of ≈829 and ≈232, which correspond to the monopole and dipole resonances of BHMR, respectively. The insets in Figure 2b represent the phase distributions in the BHMR at resonances. At 624 Hz, the phase profile of acoustic field in the BHMR shows a pattern of the monopole Mie resonance. At 1214 Hz, the phase distributions in the upper half part and lower half part of the BHMR are out of phase with each other, which corresponds to a dipole-like Mie resonance.[9,10] The monopole and dipole modes are due to the Willis coupling between the upper and lower parts of the BHMR.[16,17] Meanwhile, the emission efficiencies of the monopole and dipole modes are greatly enhanced because of the minimum radiation loss at resonances. Hence the BHMR with a central monopole source excite monopole mode at 624 Hz and dipole mode at 1214 Hz, but the SMR with a central monopole source only induces two monopole resonances. In Figure 2b, the dashed–dotted line shows the acoustic enhanced efficiency (P_1/P_0) of a BHMR structure as a function of frequency when considering the thermoviscous effects. The thermoviscous acoustics module is added to calculate the acoustic field distributions, and the viscous friction and thermal diffusion are included in the curved slits of the BHMR. The dynamic viscosity of air in the elongated channel is 1.81×10^{-5} Pa s, the heat capacity at constant pressure is 1005.4 J (kg K)$^{-1}$, the thermal conductivity is 0.0258 W (m K)$^{-1}$, and the bulk viscosity is set as 1.09×10^{-5} Pa s. Two distinct peaks can be observed at ≈595 and ≈1174 Hz with the peak-values of ≈128 and ≈16, respectively. The insets show the phase distributions in BHMR at resonances, which mean the monopole and dipole modes still exist at the thermoviscous case. Therefore, the thermoviscous losses result in the decreases of both resonance frequency and enhanced efficiency of BHMR, but the monopole and dipole modes are still well preserved with thermoviscous losses included, which are consistent with the previous reports.[7,8]

Next, we study the acoustic field distributions and the far-field radiations of the monopole and dipole antennas by the BHMR. In **Figure 3**, the first and second columns show the simulated acoustic pressure fields and directivity patterns at 624 Hz, respectively. The third and fourth columns represent the acoustic pressure fields and directivity patterns at 1214 Hz, respectively. A monopole source is located at the center with amplitude of 1 N m^{-2}. Figure 3a,b shows the simulated results of a monopole source in free space at 624 and 1214 Hz, respectively. It is observed that the radiated energy of the monopole source is localized in near-field and the far-field radiation efficiency is extremely low. Figure 3c,d shows the simulated results of a monopole source centered in a BHMR at 624 and 1214 Hz,

**ADVANCED
SCIENCE NEWS**
www.advancedsciencenews.com

**ADVANCED
MATERIALS
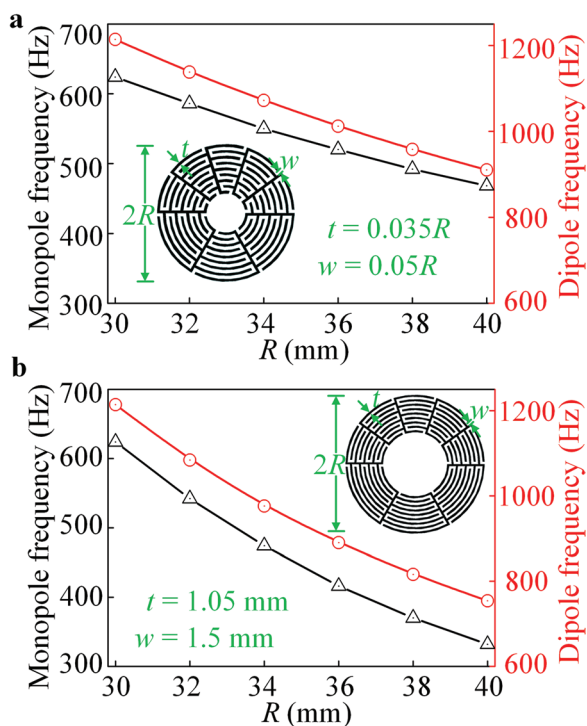TECHNOLOGIES**
www.advmattechnol.de

Figure 3. The first and second columns show the simulated acoustic pressure fields and directivity patterns at 624 Hz, respectively. The third and fourth columns represent the acoustic pressure fields and directivity patterns at 1214 Hz, respectively. Simulated results of a monopole source in free space at a) 624 Hz and b) 1214 Hz. Simulated results of a monopole source centered in a BHMR at c) 624 Hz and d) 1214 Hz. Simulated results of a monopole source enclosed by the equivalent BHMR at e) 624 Hz and f) 1214 Hz.

respectively. At 624 Hz, an enhanced monopole response is observed and the far-field radiation pattern has an omnidirectional distribution with the enhancement of ≈30 dB. At 1214 Hz, the monopole source in the BHMR is converted into an enhanced dipolar antenna. The acoustic pressure fields on the left and right sides of the BHMR have equal high strength but opposite phase. The corresponding radiation pattern shows an enhancement of ≈30 dB, while the radiation directivity is maximal along the horizontal direction and minimal along the vertical direction. Figure 3e,f shows the simulated results of a monopole source enclosed by the equivalent BHMR based on Equation (1) at 624 and 1214 Hz, respectively, which match well with the results in Figure 3c,d. The simulations demonstrate that the BHMR can modify the ambient environment of the monopole source to achieve both enhanced monopole and dipole antennas. So far, various strategies, such as phononic crystals,[3,27,28] surface gratings with subwavelength slits,[5,29,30] and acoustic Mie resonant metamaterials[25,31,32] have been proposed to realize acoustic antennas. In general, the monopole source only induces the monopole resonance and the dipole source excites the enhanced dipole radiation.[7,8,25] The simultaneously enhanced monopole and dipole radiations by a monopole source cannot be achieved by previous structures. Our BHMR structure provides a new approach for the design of acoustic antennas that realizes both enhanced monopole and dipole acoustic emissions with well-preserved directivity. Meanwhile, the BHMR structure is miniature with a deep-subwavelength dimension and takes the advantages of simple and compact design compared with the existing methods.

We further study the dependence of the resonance frequency of the BHMR on the structure size. In **Figure 4**a, the triangle scatters for the left-hand scale and the circle scatters for the right-hand scale show the simulated monopole and dipole resonance frequencies as a function of the outer radius R, respectively. Here, the wall thickness t and the channel width w are set as $0.035R$ and $0.05R$, respectively. It is found that the monopole resonance frequency decreases from ≈624 to ≈468 Hz, while the dipole resonance frequency decreases from ≈1214 to ≈910 Hz with increasing R from 30 to 40 mm. Such variations are analogous to that of the isotropic Mie resonators whose resonance frequency is given as $f = \frac{c_{air}}{\pi n_r}\sqrt{\frac{2\eta}{R_i(R-R_i)}}$, where n_r is the effective refractive index and η is the filling ratio of air channels.[24,26] The increased R results in the decreased resonance frequencies. Figure 4b shows the variations of the monopole (triangle scatters) and dipole resonance frequencies (circle scatters) with R. Here, the wall thickness t and channel width w are fixed as 1.05 and 1.5 mm, respectively. In this case, the shell thickness $(R-R_i)$ is unchanged. With increasing R from 30 to 40 mm, the monopole resonance frequency decreases from ≈624 to ≈332 Hz, while the dipole resonance frequency decreases from ≈1214 to ≈754 Hz. The decreased resonance frequencies of the monopole and dipole modes are due to the increased n_r, increased R_i, and decreased η. Thus, the monopole and dipole resonance frequencies can be decreased to the lower frequency range by increasing the size of BHMR.

**ADVANCED
SCIENCE NEWS**
www.advancedsciencenews.com
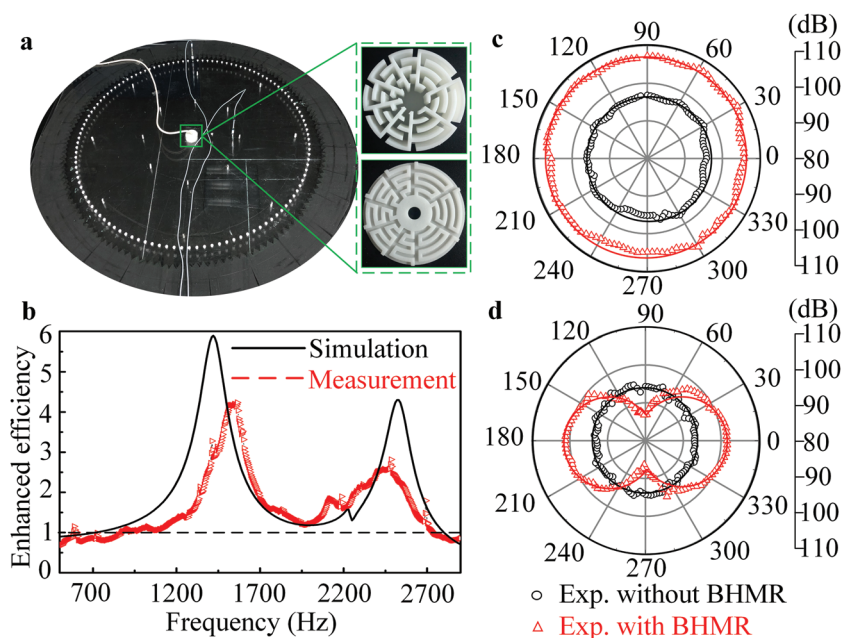
**ADVANCED
MATERIALS
TECHNOLOGIES**
www.advmattechnol.de

Figure 4. a) Simulated monopole (triangle scatters) and dipole (circle scatters) resonance frequencies as a function of the outer radius R. Here, the wall thickness t and the channel width w are set as $0.035R$ and $0.05R$, respectively. b) Variations of the monopole (triangle scatters) and dipole resonance frequencies (circle scatters) with R. Here, the wall thickness t and the channel width w are fixed as 1.05 and 1.5 mm, respectively.

acoustic field distributions and the step size along the circumference with radius of 550 mm is $\Delta\theta = 3°$. Another identical microphone was used for phase reference. In Figure 5b, the triangle scatters show the measured enhanced efficiency of the BHMR sample as a function of frequency. Here, the enhanced efficiency was given by the ratio of measured acoustic pressure at the position of (550 mm, 0) with BHMR sample to that without BHMR sample. It was observed that two distinct peaks appear at ≈1530 and ≈2440 Hz, respectively, which correspond to the enhanced monopole and dipole antennas. For better comparison, the solid line in Figure 5b represents the simulated result considering thermoviscous dissipation. The simulated monopole and dipole emissions occur at ≈1440 and ≈2520 Hz, respectively. The measured results matched well with the simulated results, while some deviations between the measurement and simulation should be ascribed to the sample fabrication error and the instability of sound source. In Figure 5c, the triangle scatters and circle scatters show the measured acoustic pressure fields with and without BHMR sample at 1530 Hz, respectively. The results were measured at the circumference with radius of 550 mm. The solid curves were given as references. In this case, the acoustic monopole mode shows well-preserved omnidirectional radiation with an enhancement of about 10 dB in the presence of BHMR sample. Figure 5d shows the measured acoustic pressure fields with (triangle scatters) and without (circle scatters) BHMR sample at 2440 Hz. At this frequency, the monopole source was converted into an enhanced dipole antenna with radiation directivity and the maximal enhancement reached about 10 dB. The experimental results further confirm the effectiveness of the BHMR in generating both enhanced monopole and dipole antennas.

4. Experimental Section

Finally, the enhanced monopole and dipole antennas were experimentally verified by the proposed BHMR. **Figure 5**a shows the photograph of the experimental setup. The BHMR sample was sandwiched between two parallel plexiglass plates ($1500 \times 1500 \times 8$ mm³) with a space of 20 mm and the enlarged drawing showed the details of the BHMR sample. By using 3D printing technology, the BHMR sample was made of UV resin with mass density of 1400 kg m⁻³ and sound speed of 1950 m s⁻¹. Because of the large thermoviscous dissipations in the narrow channels and the easy deformation in the sample fabrication, the experimental sample was different from that in the simulations. Here, the curling number N of the BHMR sample is set as 4, the outer radius is $R = 29.52$ mm, the wall thickness is $t = 2.14$ mm, and the channel width is $w = 3.27$ mm. A central point source was launched from a narrow tube connected to a loudspeaker. Sound absorbing foams were placed on the edges of the plexiglass plates to reduce sound reflections. A microphone (1/4 in., B&K type-4938) was used to scan the

Figure 5. a) Photograph of the experimental setup. The enlarged drawing shows the details of the BHMR sample. b) Measured (triangle scatters) and simulated (solid line) acoustic enhanced efficiency of the BHMR sample as a function of frequency. c) Measured acoustic pressure fields with (triangle scatters) and without (circle scatters) BHMR sample at 1530 Hz. d) Measured acoustic pressure fields with (triangle scatters) and without (circle scatters) BHMR sample at 2440 Hz. The solid curves are given as references.

1900970 (5 of 6)

5. Conclusion

In conclusion, a subwavelength BHMR is proposed to realize both enhanced low-frequency monopole and dipole acoustic antennas. The monopole sound source at the center of BHMR can excite monopole and dipole modes at certain frequencies. The simulated acoustic field distributions and the radiation patterns demonstrate the existences of monopole and dipole responses in the BHMR. It is found that the acoustic resonances and Willis couplings of BHMR together contribute to the enhanced monopole and dipole sound antennas. In addition, we study the effects of the structure size on resonance frequencies, and find both monopole and dipole resonances decrease to the lower frequencies with increasing the size of BHMR. Finally, we experimentally confirm the generation of enhanced monopole and dipole responses from the BHMR, and reveal that the enhancement of the acoustic monopole mode can reach ≈10 dB and the dipole emission has an enhancement of ≈10 dB. The BHMR structure can also be constructed by different numbers of fanlike labyrinth units. In addition, we think that the present mechanism of producing enhanced monopole and dipole emissions via the BHMR can be extended to underwater acoustic radiations in principle. The bianisotropic metamaterials and emission enhancements also could be extended to the electromagnetic wave radiations, but some special designs are needed. The proposed BHMR structure provides an alternative method for enhanced low-frequency sound radiations, which may be anticipated in loudspeaker design and acoustic communication.

Conflict of Interest

The authors declare no conflict of interest.

[1] W. Lee, H. C. Kim, Y. J. Jung, Y. A. Chung, I. U. Song, J. H. Lee, S. S. Yoo, *Sci. Rep.* **2016**, *6*, 34026.
[2] Y. Zhang, Z. C. Song, X. Y. Wang, W. W. Cao, W. W. L. Au, *Phys. Rev. Appl.* **2017**, *8*, 064002.
[3] Z. W. Zhang, Y. Tian, Y. H. Wang, S. X. Gao, Y. Cheng, X. J. Liu, J. Christensen, *Adv. Mater.* **2018**, *30*, 1803229.
[4] P. M. C. Morse, K. U. Ingard, *Theoretical Acoustics*, Princeton University, Princeton, NJ **1968**.
[5] L. Quan, X. Zhong, X. Z. Liu, X. F. Gong, P. A. Johnson, *Nat. Commun.* **2014**, *5*, 3188.
[6] K. Song, S. H. Lee, K. Kim, S. Hur, J. Kim, *Sci. Rep.* **2015**, *4*, 4165.
[7] M. Landi, J. J. Zhao, W. E. Prather, Y. Wu, L. K. Zhang, *Phys. Rev. Lett.* **2018**, *120*, 114301.
[8] J. J. Zhao, L. K. Zhang, Y. Wu, *J. Acoust. Soc. Am.* **2017**, *142*, EL24.
[9] X. D. Fan, Y. F. Zhu, B. Liang, J. C. Cheng, L. K. Zhang, *Phys. Rev. Appl.* **2018**, *9*, 034035.
[10] F. M. Liu, W. P. Li, M. Z. Ke, *Phys. Rev. Appl.* **2018**, *10*, 054031.
[11] M. B. Muhlestein, C. F. Sieck, A. Alù, M. R. Haberman, *Proc. R. Soc. A* **2016**, *472*, 20160604.
[12] S. Koo, C. Cho, J. H. Jeong, N. Park, *Nat. Commun.* **2016**, *7*, 13012.
[13] M. B. Muhlestein, C. F. Sieck, P. S. Wilson, M. R. Haberman, *Nat. Commun.* **2017**, *8*, 15625.
[14] X. S. Su, A. N. Norris, *Phys. Rev. B* **2018**, *98*, 174305.
[15] Y. Q. Liu, Z. X. Liang, J. Zhu, L. B. Xia, O. Mondain-Monval, T. Brunet, A. Alù, J. Li, *Phys. Rev. X* **2019**, *9*, 011040.
[16] C. F. Sieck, A. Alù, M. R. Haberman, *Phys. Rev. B* **2017**, *96*, 104303.
[17] L. Quan, Y. Ra'di, D. L. Sounas, A. Alù, *Phys. Rev. Lett.* **2018**, *120*, 254301.
[18] A. Merkel, V. R. García, J. P. Groby, J. Li, J. Christensen, *Phys. Rev. B* **2018**, *98*, 201102(R).
[19] B. I. Popa, Y. X. Zhai, H. S. Kwon, *Nat. Commun.* **2018**, *9*, 5299.
[20] J. Li, C. Shen, A. Díaz-Rubio, S. A. Tretyakov, S. A. Cummer, *Nat. Commun.* **2018**, *9*, 1342.
[21] J. Li, A. Díaz-Rubio, C. Shen, Z. Jia, S. Tretyakov, S. A. Cummer, *Phys. Rev. Appl.* **2019**, *11*, 024016.
[22] A. Melnikov, Y. K. Chiang, L. Quan, S. Oberst, A. Alù, S. Marburg, D. Powell, *Nat. Commun.* **2019**, *10*, 3148.
[23] L. Quan, D. L. Sounas, A. Alù, *Phys. Rev. Lett.* **2019**, *123*, 064301.
[24] Y. Cheng, C. Zhou, B. G. Yuan, D. J. Wu, Q. Wei, X. J. Liu, *Nat. Mater.* **2015**, *14*, 1013.
[25] J. J. Zhao, R. Al Jadhali, L. K. Zhang, Y. Wu, *Sci. Rep.* **2018**, *8*, 1018.
[26] C. Zhou, B. G. Yuan, Y. Cheng, X. J. Liu, *Appl. Phys. Lett.* **2016**, *108*, 063501.
[27] M. Z. Ke, Z. Y. Liu, P. Pang, C. Y. Qiu, D. G. Zhao, S. S. Peng, J. Shi, W. J. Wen, *Appl. Phys. Lett.* **2007**, *90*, 083509.
[28] J. Qian, H. X. Sun, S. Q. Yuan, X. J. Liu, *Appl. Phys. Lett.* **2019**, *114*, 013506.
[29] Y. Zhou, M. H. Lu, L. Feng, X. Ni, Y. F. Chen, Y. Y. Zhu, S. N. Zhu, N. B. Ming, *Phys. Rev. Lett.* **2010**, *104*, 164301.
[30] Y. Cheng, J. Y. Xu, X. J. Liu, *Appl. Phys. Lett.* **2010**, *96*, 071910.
[31] G. X. Lu, E. L. Ding, Y. Y. Wang, X. Y. Peng, J. Cui, X. Z. Liu, X. J. Liu, *Appl. Phys. Lett.* **2017**, *110*, 123507.
[32] J. Zhang, Y. Cheng, X. J. Liu, *Sci. Rep.* **2018**, *8*, 10049.